Deep-Learning-Based Source Reconstruction Method Using Deep Convolutional Conditional Generative Adversarial Network

He Ming Yao[®], Member, IEEE, Lijun Jiang[®], Fellow, IEEE, and Michael Ng, Senior Member, IEEE

Abstract—This article proposes a novel deep-learning (DL)based source reconstruction method (SRM). The proposed DL-based SRM employs the deep convolutional conditional generative adversarial network (DCCGAN), which only demands one-transmitter single-frequency far-field measurement on electromagnetic (EM) scattered field as its input and further predicts the equivalent source on target scatterers. The proposed DCCGAN includes the generator (G) with an EM forward simulator and the corresponding discriminator (D), both consisting of the complex-valued deep convolutional neural networks (DConvNets). During the offline training, the generator learns the distribution between the measured scattered field data and the corresponding equivalent source on target scatterers, while the discriminator determines whether the presented equivalent sources are real or fake. Therefore, the proposed DCCGAN can generate the unknown equivalent source from measured scattered field data, by learning the distribution between the known equivalent sources and their corresponding field. Furthermore, the proposed DL-based SRM can overcome the limitation of conventional methods, involving high computational cost and strong ill-conditions. Consequently, the proposed DL-based SRM can realize the reconstruction of the equivalent source with higher accuracy and lower computation complexity. Numerical examples have demonstrated the feasibility of the proposed DL-based SRM, which opens the new path for DL-based EM computation approaches.

Index Terms— Convolutional neural network (ConvNet), deep learning (DL), real time, source reconstruction method (SRM).

Manuscript received 22 August 2023; accepted 18 September 2023. Date of publication 18 March 2024; date of current version 7 May 2024. This work was supported in part by the Research Grant Council of Hong Kong [General Research Fund (GRF)] under Grant 17207114, Grant 17210815, Grant 12300218, Grant 12300519, Grant 17201020, Grant 17300021, Grant C1013-21GF, Grant C7004-21GF, Grant 12306616, and Grant 12200317; in part by Joint Natural Science Foundation of China-Research Grants Council (NSFC-RGC) under Grant N-HKU769/21; in part by the Asian Office of Aerospace Research and Development (AOARD) under Grant FA2386-17-1-0010; in part by NSFC under Grant 61271158; in part by Hong Kong University Grants Committee (UGC) under Grant AoE/P-04/08; in part by The University of Hong Kong (HKU) under Grant 104005583; in part by the Research Grants Council of the Hong Kong Special Administrative Region, China, under Grant HKU PDFS2122-7S05; and in part by the Hong Kong Research Grants Council (HKRGC) Collaborative Research Fund (CRF) under Grant C7004-21GF. (Corresponding authors: Lijun Jiang; Michael Ng.)

He Ming Yao is with the Department of Mathematics, The University of Hong Kong, Hong Kong, China (e-mail: yaohmhk@connect.hku.hk).

Lijun Jiang is with the Department of Electronic Engineering, The Chinese University of Hong Kong, Hong Kong, China (e-mail: ljjiang@ee.cuhk.edu.hk).

Michael Ng is with the Department of Mathematics, Hong Kong Baptist University, Hong Kong, China (e-mail: michael-ng@hkbu.edu.hk).

Color versions of one or more figures in this article are available at https://doi.org/10.1109/TMTT.2024.3369420.

Digital Object Identifier 10.1109/TMTT.2024.3369420

I. INTRODUCTION

OURCE reconstruction methods (SRMs) are pivotal in electromagnetic (EM) field transformation applications [1], [2], [3], [4]. The fundamental aim is to deduce the equivalent current sources within objects of interest by analyzing measured EM data [1], [2]. Such tasks are embodied in SRM, emblematic of inverse problems in the EM domain, which necessitates the unraveling of integral equation sets that correlate with the radiative EM fields [3], [4]. By interpreting the EM fields scattering from these targets, it becomes possible to estimate the spatial distribution of these internal EM sources [1], [2], [3], [4]. Armed with this information about the equivalent sources, one can adeptly tackle a variety of EM challenges, involving testing for source discrepancies, converting between far-field (FF) and near-field (NF) measurements, and pinpointing areas of intense EM activity [3], [4], [5].

SRMs typically entail the determination of an equivalent source by resolving a series of integral equations. Over recent years, a plethora of strategies for deducing these equivalent sources has emerged, involving the genetic algorithm (GA) [6], the Bayesian inference approach [7], along with various deterministic techniques [8], [9]. Nonetheless, traditional approaches are frequently plagued by challenges of ill-posedness, a consequence of factors such as sparse EM field data pertaining to the targets under study, data perturbed by noise, and inherent smoothness of forward problem induced by integral transformations. In addition, iterative optimization techniques often require substantial computational resources to achieve an equivalent source reconstruction of acceptable precision [10], [11], [12]. As a result, the practicality of many traditional SRMs in meeting the demands of real-time applications is questionable. In scenarios that demand extreme computation, the process could involve handling millions of variables, leading to significant memory usage and extended CPU processing intervals [1], [2], [3], [4], [5], [6], [7], [8], [9], [10], [11], [12]. Furthermore, most conventional methods require multiple measurements at multiple frequencies, increasing the data collection workload and computational burden [1], [2], [3], [4], [5], [6], [7], [8], [9], [10], [11], [12]. Most conventional SRMs also rely on NF EM data measurements, which pose stricter and more challenging requirements compared to FF measurements. Therefore, achieving high efficiency and accuracy in equivalent source reconstruction, particularly for real-time application scenarios, remains a significant challenge.

0018-9480 © 2024 IEEE. Personal use is permitted, but republication/redistribution requires IEEE permission. See https://www.ieee.org/publications/rights/index.html for more information.

Recent advancements in computational methodologies have seen an upsurge in the application of machine learning (ML) algorithms to enhance traditional EM approaches [13], [14]. Notably, there has been a surge in the utilization of deep learning (DL) strategies [15]. This trend is evidenced by a growing corpus of impactful use cases spanning diverse areas such as computational science [16], [17], [18], [19], [20], integrated field-circuit simulation [21], [22], and microwave imaging [23], [24], [25], [60], [61], [62], [63], [64]. Indeed, ML strategies have been employed to realize equivalent source reconstruction [4], [26], [27], [28]. Within these DL frameworks, the algorithms "learn" from EM data derived from traditional methodologies and do further prediction for the new application scenarios with a large number of unknowns. In [4], the convolutional neural networks (ConvNets) have been harnessed to approximate the equivalent sources of specific objects. For the ConvNets model to function accurately, the characteristics of the target and its response to certain known incident EM waves must be predefined. This preconditioning implies that the ConvNets model is specialized for predicting the equivalent sources for the same object domain when subjected to novel incident angles. Moreover, Yao et al. [26] introduced a ConvNet-based framework to facilitate equivalent source reconstruction. Nevertheless, the deployment of this DL model is limited to previously characterized scatterers, rendering the model a sophisticated numerical interpolator for EM datasets. In [27], equivalent sources were deduced for EM emissions emanating from printed circuit boards (PCBs), utilizing data derived from close-proximity field measurements. Conversely, Yao et al. [28] outline a DL-driven approach for forward EM modeling, aimed at calculating the comprehensive EM field to infer the equivalent sources. The training of such models, however, relies heavily on data collected from extensive measurements conducted at various instances and potentially across multiple frequencies. This requirement amplifies the complexity and labor-intensiveness of data collection, thus posing practical challenges for real-world application scenarios. In fact, compared with multifrequency measurements, the single-frequency measurements have many advantages: 1) the acquisition process for multifrequency measurements is more labor-intensive and complex, which might not be practical in certain scenarios and 2) the computational complexity increases significantly when incorporating multifrequency data into the DL-based model, making it challenging to achieve real-time performance. All in all, compared with conventional methods, the introductions of DL techniques have greatly speeded up the solving process of equivalent source and have greatly improved its flexibility in modeling different application scenarios.

In this work, a novel DL-based SRM is proposed based on the deep convolutional conditional generative adversarial network (DCCGAN). This proposed DCCGAN makes use of the generator (*G*) with an EM scattering simulator and the corresponding discriminator (*D*). While both the generator and the discriminator consist of the deep convolutional neural networks (DConvNets), they only utilize EM scattered field data, which is gathered using a single-transmitter, multireceiver setup at a solitary frequency in the FF region, to achieve the reconstruction of equivalent source on the intended scatterers.

The general working mechanism for this DL-based SRM is as follows.

- Off-Line Training: The generator generates the equivalent source "images" of target scatterers from single-frequency one-transmitter-measured EM scattered data in the FF, while the discriminator discriminates whether the generated "images" are real or fake. The EM scattering simulator computes the EM scattered field induced by an equivalent source "generated" from the generator, so that the performance of the generator can be further improved.
- 2) Online Application: The trained generator can work as the inversion solver to obtain the equivalent source of unknown scatterer by utilizing its FF single-frequency one-transmitter-measured EM scattered data. Therefore, the proposed DL-based SRM is adept at forecasting the equivalent source utilizing only a select array of FF EM scattering measurements. This method stands in contrast to traditional SRMs, as it obviates the need for NF data acquisition and foregoes the necessity of possessing detailed contrast information about the target. In addition, the proposed DL-based model can be potentially combined with multiresolution techniques, including the iterative multiscaling approach (IMSA) [55], [56], [57], [58], [59], to alleviate both nonlinearity and ill-posedness and improve the performance.

Thanks to the power of the trained DCCGAN, the benefits of the newly developed DL-driven SRM include the following.

- Efficiency: This novel approach surpasses traditional methodologies by achieving equivalent source reconstruction with significantly reduced computational complexity and expedited processing times since using DConvNet greatly improves the efficiency of solving EM-based inversion problem and avoids calculating complicated Green's functions. Thus, it can potentially realize the real-time application.
- 2) Accuracy: The innovative DCCGAN model, despite utilizing a sparse array of received EM scattered fields, can infer targets' equivalent sources with notable precision. This is a considerable advancement over traditional techniques. Furthermore, DCCGAN's training leverages an EM scattering simulator, incorporating abundant prior knowledge. This integration allows for the impact of equivalent source on EM scattered fields to be assessed, thereby refining DCCGAN's training process. Consequently, the optimized DCCGAN is capable of reconstructing the equivalent source with impressive fidelity.
- 3) Simplicity: Our approach requires only the data from EM scattered fields obtained through a solitary transmitter at a single frequency from afar. The training phase for the DCCGAN is predicated on a straightforward synthetic dataset, yet it accounts for incident EM waves from a spectrum of random angles. Once trained, the DCCGAN is adept at reconstructing the equivalent source when subjected to EM waves from arbitrary directions during the operational phase.
- 4) Flexibility: The proposed DL-based SRM is designed to be inherently adaptable, with the capacity to assimilate

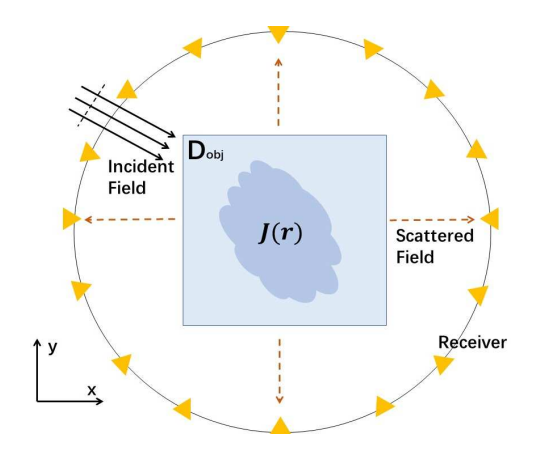


Fig. 1. Schematic of the scattering of TM wave from a dielectric region $D_{\rm obj}$.

a wide range of prior information into its framework. Because the training data in the off-line step can be created according to prior information, the proposed process itself does not need much change to handle it universally. This certainly provides the most flexibility in using the proposed DL-based SRM.

5) Extensibility: In practical applications, it is common for new, real-time measurements of unknown EM sources to be collected. The proposed DL method allows for the seamless integration of these new data points into the training dataset, effectively expanding the dataset required for training the DL algorithm. This extensibility ensures that our model remains up-to-date and adaptable, as it can continuously learn from new measurements and improve its accuracy and performance over time. This advantage makes our method a valuable tool for EM source reconstruction in dynamic and evolving scenarios.

II. THEORY AND FORMULATION

A. Problem Formulation

Fig. 1 illustrates the schematic setup for the equivalent source reconstruction process. Here, a target region is surrounded by M receivers. A single TM-polarized wave, denoted as E^{in} , originating from a unique direction (with the incident wave count N_i set to 1), illuminates the specified target area (D_{obj}) . Surrounding this target area, the M receivers are strategically positioned to capture the EM scattering wave emanations. In fact, for each set of equivalent source on scatterer, there is only one incident wave illuminating them, i.e., $N_i = 1$. D_{obj} is segmented into a grid of $N \times N$ cells, allowing for the reconstruction of the equivalent source at each discrete cell using the captured EM field data. Typically, the grid resolution—reflected by the number of cells—exceeds the quantity of receivers encircling the region. This depiction utilizes a 2-D framework to elucidate the workings of our proposed technique; however, it is important to underscore that the methodology is equally applicable to 3-D configurations. As a typical EM inversion problem, this work employs the received EM field to realize source reconstruction [1], [2], [3], [4], [5].

In detailing the comprehensive methodology for equivalent source reconstruction, the foundational principles are encapsulated within equations designated as (1) and (2). These are Authorized licensed use limited to: Missouri University of Science and Technology. Downloaded on January 16,2025 at 18:24:03 UTC from IEEE Xplore. Restrictions apply.

referred to as the Lippmann–Schwinger equations, cited in [1], [2], [3], [4], and [5]. Specifically, the following equation serves as the state equation, delineating the interplay between the fields scattered within the domain D_{obi} :

$$E^{\text{in}}(\mathbf{r}) = E^{t}(\mathbf{r}) - k_0^2 \int_{D_{\text{obj}}} G(\mathbf{r}, \mathbf{r}') \chi(\mathbf{r}') E^{t}(\mathbf{r}') d\mathbf{r}' \qquad (1)$$

where Green's function is $G(\mathbf{r}, \mathbf{r}') = -(j/4)H_0^{(2)}(k_0|\mathbf{r} - \mathbf{r}'|)$, while $H_0^{(2)}$ represents the Hankel function of the second kind and zeroth order, and k_0 denotes the wavenumber in a vacuum. The locations $\mathbf{r}' = (x', y')$ and $\mathbf{r} = (x, y)$ correspond to the source and observation points within D_{obj} , respectively. The total EM field is symbolized by E^t , and the contrast function is defined as $\chi(\mathbf{r}') = \varepsilon_r(\mathbf{r}') - 1$ [23], [24], [25].

The subsequent equation, pivotal to the EM scattering paradigm, is identified as the data equation. This equation delineates the relationship between the scattered electric field E^s and the total electric field E^t , as expressed in the following equation:

$$E^{s}(\mathbf{r}) = k_0^2 \int_{D_{\text{obj}}} G(\mathbf{r}, \mathbf{r}') \chi(\mathbf{r}') E^{t}(\mathbf{r}') d\mathbf{r}'$$
 (2)

where $r = (x_R, y_R)$ denotes the receiver locations, and r' =(x', y') represents the coordinates for segments within D_{obj} .

In the exposition of source reconstruction concepts, we introduce the term "equivalent current," alternatively known as the "contrast current," which is complex-valued and has real and imaginary parts. We represent it as J(r') = $\chi(\mathbf{r}')E^{t}(\mathbf{r}')$ [1], [2], [3], [4], [5]; thus, (2) is rewritten to be

$$E^{s}(\mathbf{r}) = k_0^2 \int_{D_{\text{obj}}} G(\mathbf{r}, \mathbf{r}') J(\mathbf{r}') d\mathbf{r}'.$$
 (3)

The final target of reconstructing the equivalent source is to compute the equivalent source in the objective domain $D_{\rm obj}$ under one incident field from M transmitters around the D_{obj} . However, solving (2) directly to compute the equivalent source is very hard [1], [2], [3], [4], [5], [6], [7], [8], [9], [10], [11], [12]. In the traditional approaches, (3) is first written into the following discretized equation [1], [2], [3], [4], [5], [6], [7], [8], [9], [10], [11], [12] as matrix form, in which D_{obi} is uniformly discretized into pieces. Meanwhile, the equivalent source in an individual piece can be seen as the piecewise constant

$$\overline{E^s} = \overline{\overline{G_D}} \cdot \overline{\overline{\chi}} \cdot \overline{E^t}
= \overline{\overline{G_D}} \cdot \overline{J}$$
(4)

where the matrices $\overline{\overline{G_D}}$ have the size of $N^2 \times N^2$ and $\overline{\overline{G_D}}$ = $k_0^2 S_{n'} G(\boldsymbol{r}_n, \boldsymbol{r}_{n'})$, where $S_{n'}$ denotes the area of each source cell. Here, $n = 1, ..., N^2$ and $n' = 1, ..., N^2$. In addition, the discrete representations are denoted as follows: \bar{E}^s for the scattered field, \bar{E}^t for the total field that corresponds, $\bar{\chi}$ for the contrast, and \bar{J} symbolizes the equivalent source.

Unfortunately, N^2 is usually much larger than M (for source reconstruction task, the case is more extreme because there is only one incident wave corresponding to a set of received scattered EM field, i.e., $N_i = 1$). Addressing (4) with conventional techniques presents difficulties due to the scarcity of received EM field data [1], [2], [3] and also usually suffers from the relatively high computation complexity [1], [2], [3], [4], [5], [6], [7], [8], [9], [10], [11], [12].

B. DCCGAN for Source Reconstruction

The CGAN is the typical generative model and has been widely used in various fields [28], [29], [30], of which the training can be seen as a two-player minimax game, i.e., the Nash equilibrium [29], [30], [31], [32], [33], [34]. In general, CGAN includes both the generator and the discriminator. The generator learns mapping a vector sampled from a latent space to the space of ground-truth samples [29], [30], [31], [32], [33], [34], while the discriminator learns mapping a sample to a probability that predicts if the presented "image" is real or fake. CGAN also develops the method to control the mapping from input to output by conditioning some "extra information" (e.g., the difference between the "generated" images and the ground-truthed images). Thanks to the flexibly-added "extra information," the CGAN framework presents the superiority in image-based tasks, particularly in the cases with limited input information [29], [30], [31], [32], [33], [34].

In this article, thanks to the power of CGAN, equivalent source reconstruction can be realized by using only onetransmitter single-frequency FF measurement, which greatly simplifies the measurement/simulation and decreases the computation cost. This proposed DCCGAN for source reconstruction is based on the discriminator and its corresponding generator with the EM scattering simulator for the EM scattering process. In addition, training samples for DL models are generated based on numerical simulation. The proposed DCCGAN is designed to learn the nonlinear mapping between the data distribution of scattered EM fields and the data distribution of the corresponding equivalent source on the target scatterers, based on which it can realize source reconstruction for the unknown scatterers with high accuracy in real time. The proposed DCCGAN estimates the difference and the similarity between "generated" equivalent source images and their ground truth, and also involves the difference between the EM scattered field resulted from "generated" equivalent source images and the input EM scattered field. Although the scattered field resulted from "generated" equivalent source images only originated from one single incident EM wave in a single frequency, the proposed DCCGAN can make use of this limited scattered field information to realize excellent reconstruction results.

The specific structure of the proposed DCCGAN is illustrated in Fig. 2, which includes two modules: the discriminator (D) and the generator (G) with an EM scattering simulator. The generator generates the equivalent source "images" on target scatterers from measured scattered data, while the discriminator discriminates whether the generated "images" are real or fake. The loss function of the proposed DCCGAN evaluates the difference and the similarity between the created "images" and the ground-truthed "images." Meanwhile, to make the DL structures "understand" the effect of created scatterers on the EM scattered field, its loss function also involves the misfit between the input EM scattered field E^s of the generator and that computed from EM scattering

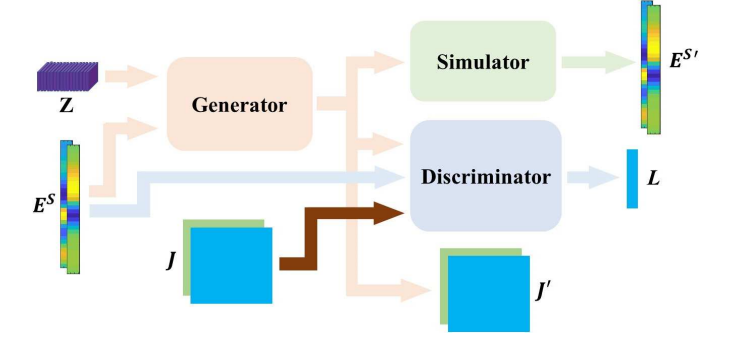


Fig. 2. Scheme of the proposed DCCGAN.

simulator, as shown in (5). This DCCGAN succeeds in reconstructing equivalent source "images" utilizing input with a smaller size, which is much challengeable for the conventional methods [6], [7], [8], [9], [10], [11], [12].

1) Discriminator: The structure of the discriminator is presented in Fig. 3. The discriminator is designed by using the complex-valued DConvNet [28], [29], [30]. Its input is the "generated" equivalent source "images" from the generator or the ground-truthed equivalent source "images," both of which are $N \times N \times 2$ complex matrix constituted by the real and imaginary parts of the equivalent source. Meanwhile, together with the ground-truthed or generated equivalent source "images," the received EM scattered field is used as the label condition for the discriminator, which has the size of $M \times 1 \times 2$ (M is the number of receivers, while $N_i = 1$ is the total number of the incident field). To concatenate the input EM scattered field and the equivalent source, the deep convolutional asymmetric encoder-decoder architecture (DCAEDA) has been used, which has demonstrated the excellent performance for the scientific computation field [35], [36]. Based on this DCAEDA, the input EM scattered field is concatenated with equivalent source "images" to capture features for the following deep convolutional structure. Based on the final classification layer, the final output discriminates the realness of the "images." In detail, the discriminator applies convolution (Conv.), Up-convolution (Up-conv.), rectified linear unit (ReLU), leaky rectified linear unit (LeReLU), and batch normalization (BN) repeatedly. In addition, the 0.2 dropout operation is used as a regularization operation to enhance prediction accuracy and to decline overfitting [37].

While the generator is trained in order to fool the discriminator, the discriminator network is trained to distinguish the reconstructed image from the true one. The specific computation process can be described as follows:

$$\min_{G} \max_{D} V(D, G)
= E_{\chi \sim p_{\text{data}(\chi)}} \left[\log D(E^{s}, J) \right]
+ E_{(E^{s}, Z) \sim p_{(E^{s}, Z)}} \left[1 - \log D(E^{s}, G(E^{s}, Z)) \right]$$
(5)

where D() represents the probability computed from the training dataset, and $D(E^s, G(E^s, Z))$ represents the probability of the generated EM sources, which are created by $G(E^s, Z)$. In addition, while Z is denoted as the noise input to the

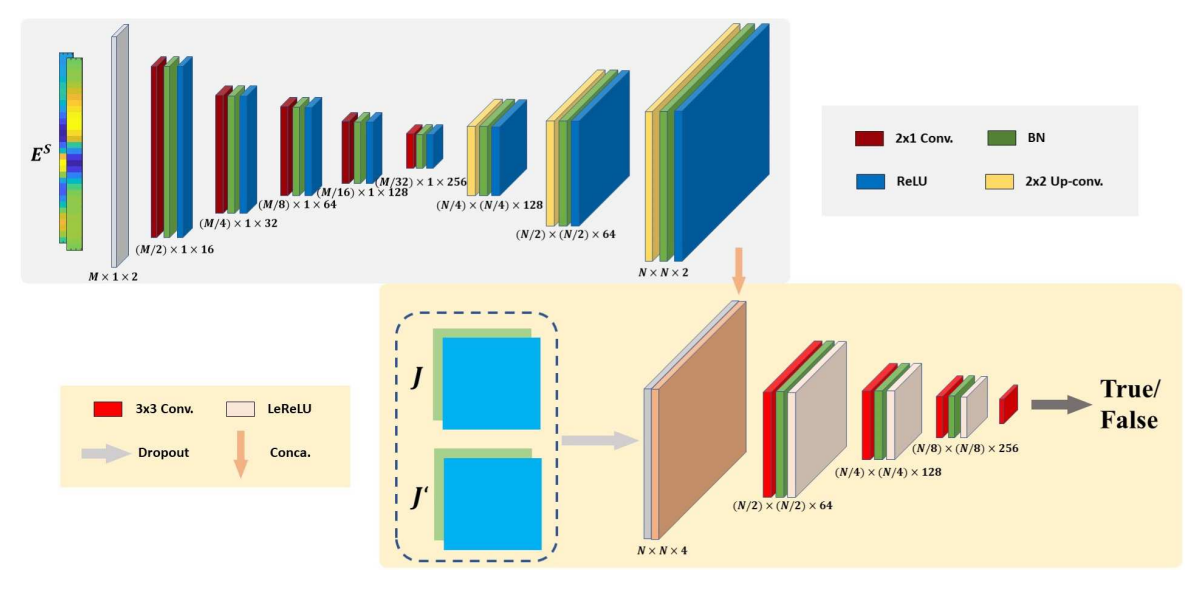


Fig. 3. Discriminator of the proposed DCCGAN. Conv. is the convolution, BN is the batch normalization, ReLU is the rectified linear unit, LeReLU is the leaky rectified linear unit, Conca. is the concatenation, and Up-conv. represents the up-convolution.

generator, (E^s, Z) is combined as the condition data input to the generator. According to this value function, the weights of the generator and discriminator should be trained and updated simultaneously to maximize the probability of accuracy in discriminating both the training dataset and samples from the generator, while training the generator to minimize $\log D(E^s, G(E^s, Z))$.

Based on (5), the specific loss function of discriminator in the training process can be defined as follows:

$$L_{D} = -\frac{1}{n} \sum_{j=1}^{n} \left[\log \left(D\left(E^{s,j}, G\left(E^{s,j}, Z^{j}\right)\right) \right) \right] - \frac{1}{n} \sum_{j=1}^{n} \left[\log \left(1 - D\left(E^{s,j}, J^{j}\right)\right) \right]$$
(6)

where n stands for the batch size, while j indicates the jth data in the batch. During the training process, the target of the discriminator is to make the score of ground truth close to 1 and that of fake inputs close to 0.

To further demonstrate the computational details of the discriminator, we divide the discriminator into two parts (as shown in Fig. 3). The first part is DCAEDA [shown in the top-left part in Fig. 3 and in (7)], where the input is the received scattered field E^s and the output X is combined with the EM source for the next part. The second part is the deep convolutional structure [shown in the bottom-right part in Fig. 3 and in (8)], where the input is the combination between X and the EM source and the output is the finally-discriminated score. The nonlinear relation is denoted as (7) and (8)

$$X = \sigma_{N_C} \left(w_{N_C} * \sigma_{N_C - 1} \left(\dots \left(w_2 * \sigma_1 \left(w_1 * E^s + d_1 \right) + d_2 \right) \dots \right) + d_{N_C} \right)$$
(7)

where w_k is the parameters of the Conv. kernel (filter weights) for the convolutional layers and of BN layers at level j ($k = 1, ..., N_C$, and $N_C = 8$ for DCAEDA in Fig. 3), while d_k are

bias terms. The functions σ_k comprises ReLU [44], [45]

$$S = \omega_{N_P} * \theta_{N_P - 1} (\dots (\omega_2 * \theta_1 (\omega_1 * [X, Dr(J)] + \beta_1) + \beta_2) \dots) + \beta_{N_P}$$
(8)

where ω_j is the parameters of the Conv. kernel (filter weights) for the convolutional layers and of BN layers at level k ($j=1,\ldots,N_P$, and $N_P=4$ for the deep convolutional structure in Fig. 3), while β_j are bias terms, while Dr() stands for the operation of dropout. The functions θ_j comprises LeReLU [29], [30], [31], [44], [45].

2) Generator: The generator of DCCGAN is implemented by adopting a new DCAEDA, which has been widely utilized in engineering computation research [35], [36]. The operation of the generator can be regarded as a transformation process, where the measured scattered field is transferred into the equivalent source on target scatterers. Fig. 4 shows the specific internal structure of the generator. Its input is a matrix with the size of the $M \times 1 \times 2$ (M is the number of receivers. $N_i = 1$ is the total number of the incident field), which stores the scattered field E^s . Thus, it is referred to as "field data." The real and imaginary parts of E^s stand for its two tubes, which is presented in Fig. 4. Its output is the real and imaginary parts of the targeted equivalent source, which is a $N \times N \times 2$ matrix.

In Fig. 4, the designed generator mainly contains three parts: the encoder, the decoder, and the projector. E^s undergoes sequential processing within the encoding framework, where it is segmented into discrete informational units. These units, once distilled, are systematically reconstructed within the decoding stages. This iterative reassembly progresses through each layer, culminating in the formation of J'. The middle projector reshapes the noise input Z into the structure to upscale the noise Z using a fully connected operation and reshapes the output to the specified size. As shown in Fig. 4, Conv., ReLU, and BN are applied repeatedly in the encoder, while Up-Conv., BN, and ReLU operations constitute the

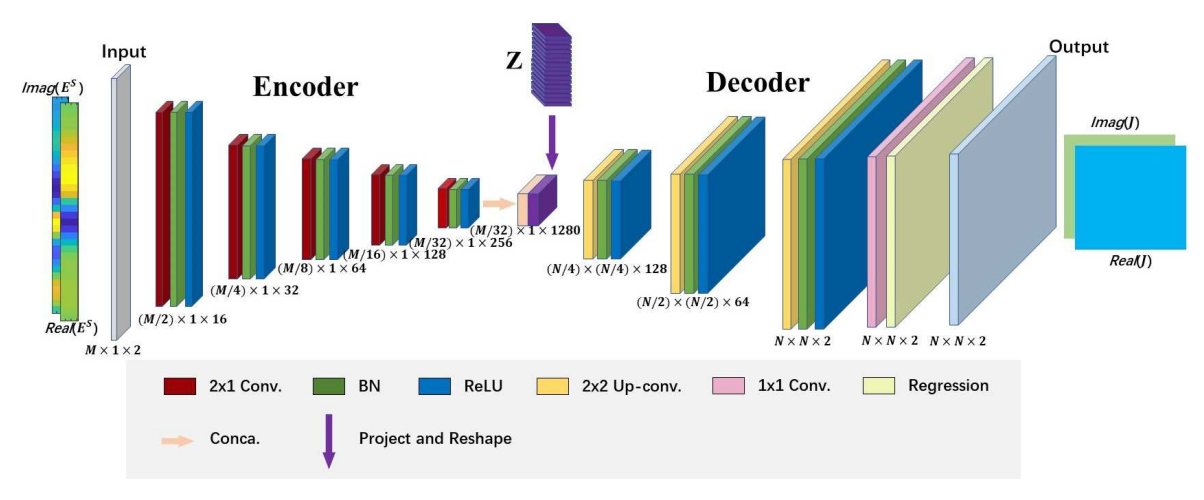


Fig. 4. Generator of the proposed DCCGAN. Conv. is the convolution, BN is the batch normalization, ReLU is the rectified linear unit, Conca. is the concatenation, and Up-conv. represents the up-convolution.

corresponding decoder. A final Conv. layer and a hyperbolic tangent layer are set at the end of the decoder

$$J' = G(E^s, Z). (9)$$

The entire process in generator can be described as a transformation process in (9), which maps the received scattered field to the equivalent source on the target scatterers. In this process, E^s is utilized as the input of the complex-valued DCAEDA, while J is chosen to be the output. In addition, the whole process of constructing the model does not need to calculate Green's function and reduce the ill-posedness of the conventional methods [6], [7], [8], [9], [10], [11], [12]. Because of prior information integrated by training, the proposed DCCGAN can alleviate the nonuniqueness [42], by offering a "better" prediction (i.e., the most possible solution). Moreover, the proposed generator can complete the reconstruction operation by only one model, which is simpler than the two-step approach [38].

To further demonstrate the computational details of the generator, we divide the generator into two parts (as shown in Fig. 4). The first part is the encoder of DCAEDA [shown in the left part in Fig. 4 and in (10)], where the input is the received scattered field E^s and the output Y is combined with the projected noise Z for the next part. The second part is the decoder of the DCAEDA [shown in the right part in Fig. 4 and in (11)], where the input is the combination between Y and projected noise Z and the output is the reconstructed EM source. The nonlinear relation is denoted as (10) and (11)

$$Y = \sigma_{N_M}(w_{N_M} * \sigma_{N_M - 1}(\dots(w_2 * \sigma_1(w_1 * E^s + d_1) + d_2)\dots) + d_{N_M})$$
(10)

where w_k is the parameters of the Conv. kernel (filter weights) for the convolutional layers and of BN layers at level k ($k = 1, ..., N_M$, and $N_M = 5$ for the encoder in Fig. 4), while d_k are bias terms. The functions σ_k comprise ReLU [44], [45]

$$J' = \omega_{N_T} * \theta_{N_T - 1}(\dots(\omega_2 * \theta_1(\omega_1 * [Y, Z] + \beta_1) + \beta_2) \dots) + \beta_{N_T}$$
(11)

where ω_j is the parameters of the Conv. kernel (filter weights) for the convolutional layers and of BN layers at level j

 $(j=1, ..., N_T, \text{ and } N_T=4 \text{ for the decoder in Fig. 4}), \text{ while } \beta_i \text{ are bias terms. The functions } \theta_i \text{ comprise ReLU [44], [45].}$

While the loss function of the generator directly defines the physical meaning and the objective of source reconstruction, the difference between prediction and true label together with the "physical" effect of the prediction on the EM scattering process has to be taken into consideration, so that the source reconstruction problems can be solved successfully. The loss function of the conventional CGAN merely consists of two terms L_C and L_p , as shown in (12) and (13). They represent the adversarial loss function used for the conventional CGAN [29], [30], but they unfortunately cannot involve the physical meaning of EM scattering. To follow the physical meaning of the source reconstruction process, we revise its conventional loss function by adding L_E and L_S , as shown in (14) and (15). While L_S estimates the similarity between the generated contrast and the ground-truthed contrast, the error between E^s and $E^{s'}$ (i.e., L_E) computed from the simulator is also added to the loss function to estimate the effect of the "image" error on the EM scattering. In other words, the quality of the predicted equivalent source "image" and its effect on EM scattering can both be evaluated in the loss function. Therefore, the full loss function L_G of the generator can be written as (16)

$$L_C = -\frac{1}{n} \sum_{j=1}^{n} \left[\log \left(1 - D(E^{s,j}, G(E^{s,j}, Z^j)) \right) \right]$$
 (12)

$$L_p = \frac{1}{n} \|J - J'\|^2 \tag{13}$$

$$L_E = \frac{1}{n} \|E^s - E^{s'}\|^2 \tag{14}$$

$$L_S = \frac{1}{n} \left(1 - \text{SSIM} \left(J - J' \right) \right) \tag{15}$$

$$L_G = L_C + \lambda_1 L_p + \lambda_2 L_E + \lambda_3 L_S \tag{16}$$

where L_C denotes the adversarial loss derived from (5). While L_p indicates the mean square error (MSE) between χ and the generated χ' , SSIM is denoted as the structural similarity [38], [39], [40], [41], [42], [43] index between χ and the generated χ' . Moreover, L_E estimates the difference

between E^s and $E^{s'}$, as shown in (14), while λ_1 , λ_2 , and λ_3 ($\lambda_1 = 5$, $\lambda_2 = 5$, and $\lambda_3 = 10$) are the weighing parameters, which represent the proportion of L_p , L_E , and L_S contributing to L_G .

Several issues of the above-proposed generator model are summarized as follows.

- 1) Complex-Valued Input With Small Size: As shown in Fig. 4, the size of the input of the generator is smaller than the existing DL structures [38], [39], [40], [41], [42], [43] because the proposed generator only needs one-transmitter single-frequency incident EM wave. Here, considering that the size of the input is reduced to $M \times 1 \times 2$ ($N_i = 1$), the size of the input will not be the same as that of the output. However, the smaller input size can help decrease the computation cost of the generator, compared with other DL-based methods [38], [39], [40], [41], [42], [43]. Moreover, the source reconstruction problem is a typical complex-valued problem. Both received EM fields and equivalent source on targets are complex values.
- 2) The Attached EM Scattering Simulator: During the generator's training phase, an integrated EM scattering simulator has been adopted to help assess the fidelity of the reconstructed equivalent sources. This simulator, designed to replicate the EM scattering process, calculates EM scattered fields originated by the predicted equivalent sources. Its primary function is to ensure the precision of EM scattered fields obtained from the predicted equivalent source "images" throughout the entire training regimen. In accordance with (4), the simulator leverages the forecast equivalent sources to perform the computations essential for the EM scattering procedure. The inclusion of this simulator enables the DCCGAN framework to account for discrepancies among scattered fields emanating by "generated" equivalent sources and those observed input fields. These discrepancies contribute to the composite loss function, which is articulated in (12) and (13).
- 3) Computational Complexity: The computational overhead of the suggested generative model is primarily governed by convolutional processes, BN, and the ReLU activation function [38], [39], [40], [41]. Given that the employed filters are of minimal size, the bulk of the computational effort is attributable to the convolutions [38], [39], [40], [41], [44]. The input dimension for the encoder stage is set at $M \times 1 \times 2$, where N_i equals 1. For each convolutional layer, R filters of size $K \times K$ are utilized, with the entire architecture comprising f layers in total. Thus, the encoder has the computation complexity as $O(MN_iK^2R^2f)$ [44], [45]. The decoder part has the same kind of operations with the encoder part but from the opposite direction. The decoder part has similar hyperparameters like filter number and size with the encoder part. Only the size of output is changed to $N \times N \times 2$. Thus, the decoder part has the computational complexity as $O(N^2K^2R^2f)$. Considering $N \gg N_i$ (i.e., $N_i = 1$). The computational complexity of the entire network is dominated by the

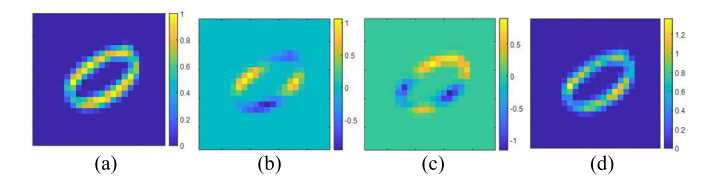


Fig. 5. Numerical setup. (a) Contrast distribution of one sample in MNIST. (b) Real part of the equivalent source J in $D_{\rm obj}$. (c) Imaginary part of the equivalent source J in $D_{\rm obj}$. (d) Magnitude of the equivalent source J in $D_{\rm obj}$.

encoder part and is approximated to be $O(N^2K^2R^2f)$ [38], [39], [40], [41], [44], [45]. In addition, the memory requirements mainly depend on the size of the filters and biases, which scales as $O(K^2R^2f)$ [38], [39], [40], [41], [44], [45].

III. NUMERICAL EXAMPLES

A. Numerical Setup and Off-Line Training

To ascertain the efficacy of the DL-based SRM, the widely recognized MNIST dataset is employed to generate a training dataset, serving as the target samples [38], [39], [40], [41], [42], [43]. In fact, MNIST has been considered as one of the most common dataset for training ML algorithms. It contains a large library of handwritten digits leading to near-human results. In this work, each sample in the MNIST dataset has the size of about $2\lambda \times 2\lambda$ (the wavelength $\lambda = 1$ m for free space) and is uniformly discretized into 24×24 pieces (i.e., N = 24). In the setup depicted in Fig. 1, TM_z waves with a random incidence angle impinge on the domain $D_{\rm obj}$, situated 30 λ away from the target area. Around $D_{\rm obj}$, in the FF region, 96 receivers are evenly spaced at a distance of 30λ , which implies that M is set to 96. For the creation of both training and testing data, we utilize fullwave EM simulations [46]. We employ the MNIST dataset to designate inhomogeneous contrast values (χ) for numeralshaped targets, varying from 0 to 1. A subset of 1000 random MNIST samples are used as scattering elements to generate the training data, comprising the scattered fields E^{s} and the equivalent currents J. The ground truth for J is determined using the conventional method of moments (MoM) [1], [2], [3], [4], [5]. Fig. 5(a) displays a sample from the training dataset. Fig. 5(b) and (c) depicts the real and imaginary components of J, respectively. For clarity, the magnitude of Jis termed an "equivalent source image," which is illustrated in Fig. 5(d). Sections III-B-III-D will employ this terminology when showcasing the DCCGAN's efficacy. It is noteworthy that the DCCGAN's offline training regimen accommodates incident waves from random directions, and its robustness against such waves will also be evaluated, with detailed results presented in Sections III-B-III-D.

Throughout the model's refinement phase, the DCCGAN framework undergoes training through the minimization of the loss function detailed in (6). This process includes assessing the discrepancies between the predicted and actual equivalent sources, as well as comparing the EM scattering fields generated by the predicted equivalent sources with the observed input EM scattering fields. The procedural steps of this training are outlined in Fig. 2. Upon completion of the

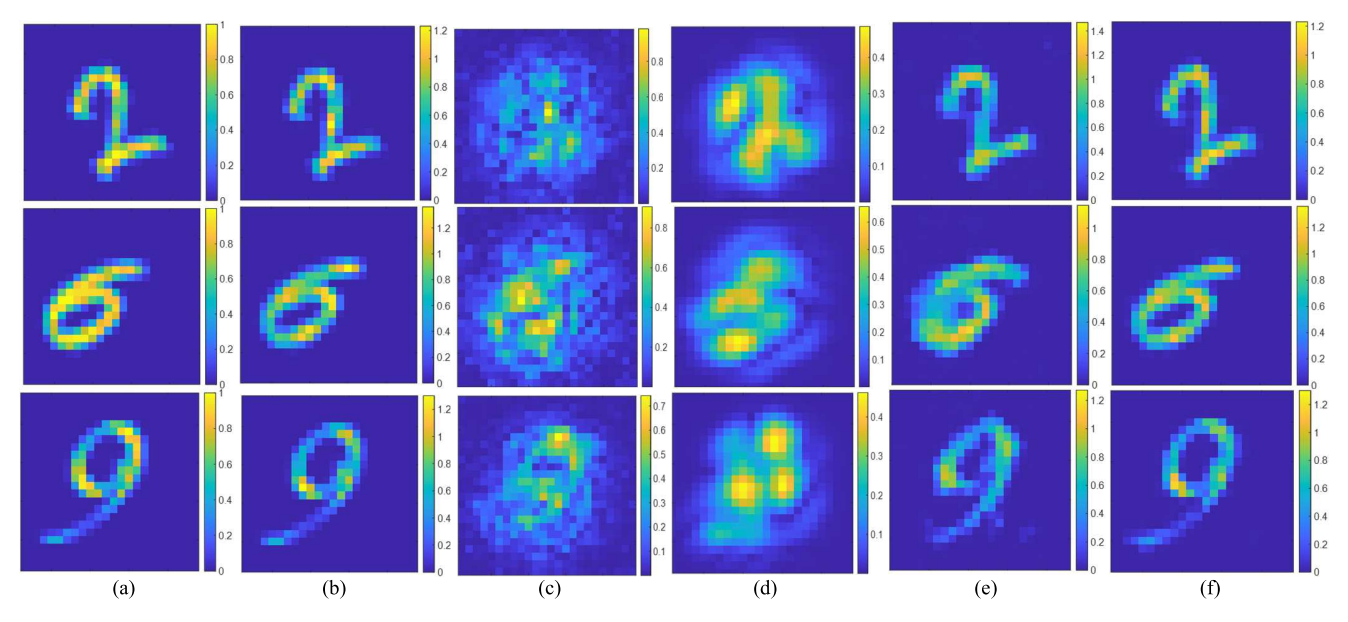


Fig. 6. Performance of the proposed DCCGAN on MNIST. (a) Contrast distribution of different number-shaped scatterers. (b) MoM result as ground truth: the computed magnitude of the equivalent source J in $D_{\text{obj.}}$ (c) MCNN result: the computed magnitude of the equivalent source J in $D_{\text{obj.}}$ (d) SDM result as ground truth: the computed magnitude of the equivalent source J in $D_{\text{obj.}}$ (e) Result from the conventional CGAN without additional loss terms: the computed magnitude of the equivalent source J in $D_{\text{obj.}}$ (f) Result from the proposed DCCGAN: the computed magnitude of the equivalent source J in $D_{\text{obj.}}$

offline training, the developed DL-based SRM is capable of accurately reconstructing equivalent sources for novel, unseen scenarios. The efficacy of this model in testing is shown in Sections III-B-III-D, with an array of diverse testing datasets applied for thorough evaluation. Both the offline training phase and the online prediction tasks of this SRM are executed using MATLAB 2021a, complemented by its DL Toolbox [47]. The optimization of the loss function is carried out with the adaptive moment estimation (Adam) optimizer. Unlike other optimizers, such as stochastic gradient descent (SGD), Adam can generally navigate through the loss surface more favorably [48]. In the assessment of "equivalent source images" discussed in Sections III-B and III-C, this study utilizes two quantifiable metrics to gauge the efficacy of the proposed DL method. These metrics are the SSIM index and the normalized mean-square error (NMSE), which are formulated in (17) and (18). These indices are widely recognized and selected as standard performance measures for evaluating DL models [38], [39], [40], [41], [42], [43], [65]

NMSE =
$$\frac{\sum_{j=1}^{J} \sum_{k=1}^{K} (x_{jk} - y_{jk})^{2}}{\sum_{j=1}^{J} \sum_{k=1}^{K} (x_{jk})^{2}}$$
(17)

where the image y is the reconstructed result of the image x. Both images have the size of $K \times J$

SSIM =
$$\frac{(2\mu_x \mu_y + C_1)(2\sigma_{xy} + C_2)}{(\mu_x^2 + \mu_y^2 + C_1)(\sigma_x^2 + \sigma_y^2 + C_2)}$$
 (18)

where regularization constants C_1 and C_2 are utilized to prevent instability in locations where the local mean or standard deviation is near zero. μ_x , μ_y , σ_x , σ_y , and σ_{xy} are the local means, standard deviations, and cross-covariance for the images x and y.

Usually, the performance of the trained DL models can be generally improved with the scale of the training dataset increasing. However, the performance improvement unavoidably slows down if the number of samples sustainedly increases. Meanwhile, with the increase in the sample number, there is surely the unavoidable computation cost resulting from the computation of samples. Thus, selecting the training dataset scale has to consider both the model performance and the computation cost. According to our trail, the chosen scale of the training dataset can better work for the training model.

Additionally, the working frequency for the proposed DCC-GAN is roughly decided by the size of $D_{\rm obj}$ [1], [2], [3], [4], [5]. The smaller size requires a relatively high frequency. Normally, if the resolution is larger, the number of training samples should be relatively larger to ensure the better performance. In other words, requiring a high resolution of target means adding more training data to ensure high performance. Thus, selecting the resolution should also take the training dataset scale into consideration.

B. Performance on Number-Shaped Objects

In this section, the application performance of the trained DCCGAN for the source reconstruction is evaluated by MNIST database. The new unknown samples in MNIST are utilized as the testing samples, as presented in Fig. 6(a). While the reference "equivalent source image" computed from MoM is shown in Fig. 6(b) as the ground truth, the corresponding "equivalent source image" of the output J is shown in Fig. 6(c). The trained DCCGAN is tested on 1000 new scatterers in the MNIST dataset. To demonstrate the capability of the proposed method, Gaussian noise (signal-to-noise ratio (SNR) = 20 dB) is added into the EM scattered field, i.e., E^s . For each test, the incident field $E^{\rm in}$ with random incident direction illuminates $D_{\rm obj}$ with a new unknown scatterer sample, as shown in Fig. 1. For the comparison, the reconstructed equivalent source calculated from the trained

TABLE I
PERFORMANCE COMPARISON BETWEEN
DCCGAN AND OTHER METHODS

| Reconstruction | MNIST | Letter | Fresnel |
|----------------|----------|----------|----------|
| DCCGAN | 0.02061s | 0.02012s | 0.02126s |
| SDM | 0.2834s | 0.2861s | 0.2819s |
| MCNN | 0.01308s | 0.01279s | 0.01292s |
| MoM | 0.6493s | 0.6515s | 0.6526s |

DCCGAN is shown in Fig. 6(f), which is much approximated to its ground truth and indicates the accuracy and validity of the proposed method for source reconstruction. As for the direction of the incident wave, incident EM fields for different directions bring different equivalent sources on the scatterers and thus different scattered fields. According to our trail, the prediction from the proposed DCCGAN can realize source reconstruction in an arbitrary incident direction, which results from the training data relying on the incident EM waves in random directions.

The comparison between the ground truth and the reconstruction from DCCGAN in Fig. 6 can prove the fact that although the new test samples have totally new shapes, the results from DCCGAN excellently agree with the ground truth. Furthermore, to increase the significance and fairness and to demonstrate the capability of the proposed DCCGAN, other popular DL-based inversion methods (i.e., the multiply-layer convolutional neural network (MCNN) [26] and the supervised descent method (SDM) [42], [43]) have also been adopted as a comparison. As presented in Fig. 6(c) and (d), MCNN can provide bad reconstruction results with little "meaningful" information, while SDM can generally provide some "meaningful" prediction and roughly describe the shape of the scatterers. Compared with the excellent reconstruction from the proposed DCCGAN, they suffer from heavy distortion and blurring outline of reconstruction. In addition, to demonstrate the effect of the designed loss function of the proposed DCCGAN, we also train the CGAN with only loss term L_C and L_p as the loss function (i.e., the loss function for the conventional CGAN [29], [30], [31]), of which the performance is illustrated in Fig. 6(e). Although the conventional CGAN can provide the approximated reconstruction, its performance still cannot be as good as that obtained from the proposed DCCGAN with the designed loss function.

Moreover, DCCGAN can save much time for completing computation than MoM and SDM, as presented in Table I. The conventional MoM uses around 0.65 s on one sample to compute an equivalent source, as illustrated in Fig. 6. In addition, MCNN and SDM utilize about 0.01 and 0.3 s, respectively, to complete reconstruction for one sample. On the contrary, the proposed DCCGAN utilizes about 0.02 s to successfully complete the reconstruction computation of one sample. Considering the bad reconstruction performance of MCNN and SDM, the proposed DCCGAN is much suitable for the real-time application.

Fig. 7(a) and (b) illustrates the comparative analysis, utilizing NMSE and SSIM, to evaluate the accuracy of the DCCGAN's predictions against the verified "equivalent source images" J. The DCCGAN's average NMSE hov-

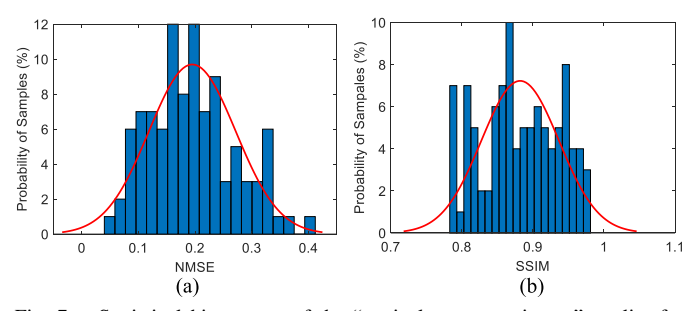


Fig. 7. Statistical histograms of the "equivalent source image" quality for the results from the DCCGAN on MNIST and fitting of its normal density function and the corresponding MoM results are used as the reference field. (a) NMSE from DCCGAN. (b) SSIM from DCCGAN.

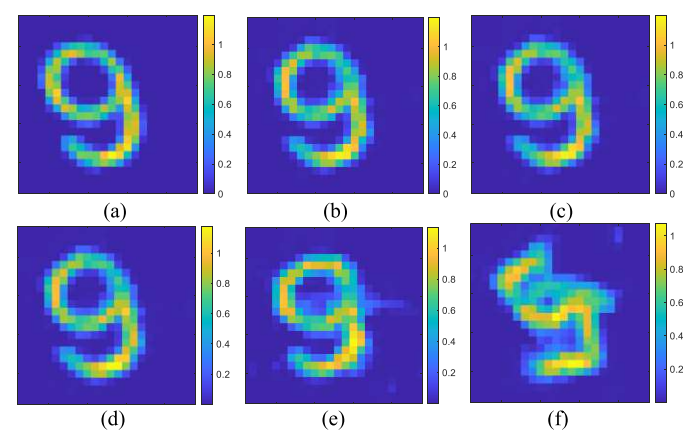


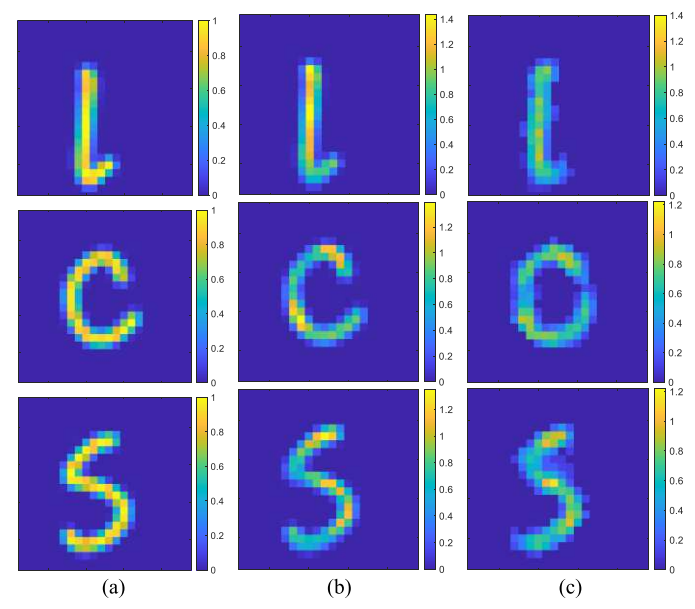
Fig. 8. One example for the sensitivity of the proposed DCCGAN on noise. (a) MoM result as ground truth: the computed magnitude of the equivalent source J in $D_{\rm obj}$. DCCGAN results with different Gauss noise levels: (b) SNR = 40 dB; (c) SNR = 30 dB; (d) SNR = 20 dB; (e) SNR = 15 dB; and (f) SNR = 10 dB.

ers around 0.19, while it achieves an average SSIM of approximately 0.89, indicating the model's proficiency in reconstructing equivalent sources with high fidelity. A detailed juxtaposition of the DCCGAN's performance with alternative methodologies is tabulated in Table I. These findings underscore the viability of the DCCGAN for deployment in real-time scenarios [1], [2], [3], [4], [5].

Furthermore, we also analyze the noise sensitivity of our proposed GAN-based model. We set the Gaussian noise to the input scattered field for the proposed DCCGAN with different SNRs: 40, 30, 20, 15, and 10 dB. As shown in Fig. 8, our proposed DCCGAN can demonstrate excellent noise tolerance. When the level of Gaussian noise achieves 15 dB, the proposed DCCGAN can still provide meaningful reconstruction result, while the reconstruction result can be much approximated to the ground truth with the noise level below 15 dB. Moreover, according to our statistical computation on the reconstruction results, the NMSE increases from 0.18 and 0.19 to 0.22 and further to 0.47 for the noise level 40, 20, 15, and 10 dB, respectively, while SSIM decreases from 0.9 and 0.89 to 0.85 and further to 0.45, which indicates the strong capability of the proposed DCCGAN.

C. Performance on Letter-Shaped Objects

Within the subsequent computational scenario, we assess the trained DCCGAN's efficacy through its application to novel

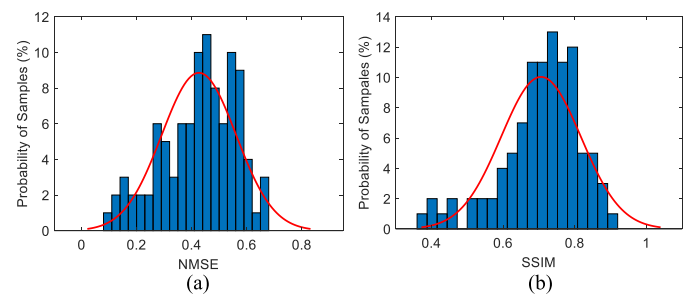


Performance of the proposed DCCGAN on "Letter." (a) Contrast distribution of different scatterers in "Letter." (b) MoM result as ground truth: the computed magnitude of the equivalent source J in D_{obj} . (c) DCCGAN result: the computed magnitude of the equivalent source J in D_{obj} .

synthetic data compilations, referred to as the "Letter" dataset. This particular dataset comprises a series of inhomogeneous scatterers, each mimicking the geometry of alphabetic characters, arbitrarily positioned within the domain D_{obi} . These letter-shaped entities each span an area measuring 2λ in both width and height. Additionally, their internal contrast values, denoted by χ , are assigned varying magnitudes within a range extending from 0 up to 1. As in Section III-B, 1000 samples in these datasets are utilized to test the trained DCCGAN. In the described experiment, a single incident electric field, E^{in} , originating from a stochastic direction, irradiates the test sample. To this incident field, Gaussian noise (SNR = 20 dB) is introduced, affecting the resultant scattered field, E^s . For the assessment of reconstructed equivalent source "images," metrics, i.e., NMSE and SSIM, have been employed. It is important to note that DCCGAN's training regimen was confined to the MNIST dataset and did not incorporate the "Letter" dataset.

Fig. 9(a) shows selected samples from the test set, whereas Fig. 9(b) displays the corresponding "equivalent source images" derived via MoM. The outcomes generated by this DL-SRM are depicted in Fig. 9(c). Despite the DL model's training being exclusively on the MNIST dataset, it was evaluated using an entirely distinct dataset. The visual comparison in Fig. 9(c) reveals a striking similarity between the DL-SRM outputs and the MoM-derived ground truth in Fig. 9(b), underscoring the model's generalization capabilities. Taking into consideration that the training of DCCGAN is based only on the MNIST dataset, the proposed method provides satisfactory results for reconstructing the equivalent source. The result also indicates the strong generality of the proposed DL-based method. Thus, despite the training of this DL method being contingent on a singular dataset, the trained DCCGAN is capable of facilitating the reconstruction of equivalent sources across disparate datasets.

Fig. 10(a) and (b) illustrates the statistical analyses for the test: the average NMSE yielded by DCCGAN is approxi-



Statistical histograms of the "equivalent source image" quality for the results from the DCCGAN on "Letter," and fitting of its normal density function and the corresponding MoM results are used as the reference field. (a) NMSE from DCCGAN. (b) SSIM from DCCGAN.

mately 0.4. Concurrently, the mean SSIM associated with the outcomes is estimated to be around 0.72, which demonstrates that the proposed approach can successfully reconstruct the equivalent source. Furthermore, DCCGAN demonstrates a swift reconstruction capability, completing the equivalent source construction for a singular scatterer in just 0.02 s. In contrast, the traditional MoM requires approximately 0.65 s to achieve a reconstruction for an identical scenario. As shown in Table I, the performance indicates the potential of the proposed DCCGAN for the real-time application.

D. Performance of Experimental Data

To further illustrate the capability of DCCGAN, we challenge DCCGAN by the widely-used experimental data measured at Institut Fresnel, Marseille, France [40], [41], [42], [43]. For the setting of this experiment, widebandridged horn antennas are employed for both transmitting and receiving antennas. While the distance between the source-object center and object-receiver is 1.67 m, eight transmitters and 241 receivers are installed. In this experiment (i.e., "FoamDielExt"), the scatterers consist of two cylinders: while the bigger one has a diameter of 0.08 m with the relative permittivity of $1.45(\pm 0.15)$, the smaller one has a diameter of 0.031 m with the relative permittivity of $3(\pm 0.3)$.

To adapt the experimental data from Fresnel into the proposed DCCGAN, we select received scattered EM field only from 96 receivers (only about 5% experimental measurement data) resulting from only one transmitter. Thus, E^s is the input of the proposed DCCGAN with M = 96, while the equivalent source J is the prediction. Then, we further test the retrained DCCGAN for the experimental data. We emphasize that only MNIST dataset is still utilized to recreate the simulationbased training data fitting this experimental setting, so that the proposed DCCGAN can be retrained for the experimental data (the process is the same as that in Section III-A). The performance of the retrained DL framework is presented in Fig. 11. DCCGAN provides the acceptable reconstruction of the experimental data. Considering the fact that only about 5% of measurement data are utilized and the training of DCC-GAN relies only on a totally different synthetic dataset, i.e., MNIST, the proposed DCCGAN demonstrates its excellent performance on realizing source reconstruction.

E. Future Works

Based on the excellent performance of the proposed DCC-GAN, it has demonstrated the potential to be applied in Authorized licensed use limited to: Missouri University of Science and Technology. Downloaded on January 16,2025 at 18:24:03 UTC from IEEE Xplore. Restrictions apply.

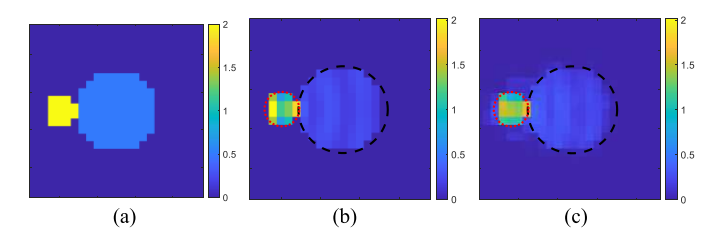


Fig. 11. Comparisons of source reconstruction for FoamDielExt. (a) Contrast distribution of FoamDielExt. (b) MoM result as ground truth: the computed magnitude of the equivalent source J in $D_{\rm obj}$. (c) DCCGAN result: the computed magnitude of the equivalent source J in $D_{\rm obj}$.

different fields related to EM source reconstruction. One of the exciting potential applications of the proposed DL-based method for EM source reconstruction is in target detection by airborne radars [49]. Our method has demonstrated promising results in overcoming the high failure rate of deterministic methods in inverse scattering, which has been a significant challenge in the field, as discussed in [49]. In the context of airborne radars, our method could be employed to improve the accuracy and reliability of target detection and tracking, especially in complex and cluttered environments. The DL model can adaptively learn the relationships between the scattered EM fields and the underlying target properties, providing a more robust and efficient solution compared to traditional deterministic approaches. Additionally, our proposed DL method can be adapted to other related areas, such as ground-based or maritime radar systems [50], [51], and can potentially be integrated with advanced radar signal processing techniques [52], to achieve even better performance in target detection and tracking.

IV. CONCLUSION

A novel SRM is proposed based on the DCCGAN. The conventional SRM unavoidably encounters various complexity and speed challenges, which makes them usually not suitable for the real-time application. The proposed DCCGAN only demands one-transmitter single-frequency FF measurement on EM scattered field and further predicts the equivalent source on target scatterers. The proposed DCCGAN employs the generator with an EM scattering simulator and the discriminator, both consisting of DConvNets. The training process of the proposed DCCGAN can be summarized as: 1) the generator learns the distribution between the measured scattered field data and the corresponding equivalent source on target scatterers and 2) the discriminator determines whether the presented equivalent sources are real or fake. Consequently, the equivalent source can be reconstructed with satisfactory accuracy and much less computational cost. Numerical examples are employed to illustrate the validity and the generality of the proposed DL-based SRM. It provides a new perspective to realize the quantitative SRM in real time.

REFERENCES

- W. C. Chew, E. Michielssen, J. M. Song, and J. M. Jin, Fast and Efficient Algorithms in Computational Electromagnetics. Norwood, MA, USA: Artech House. 2001.
- [2] M. Pastorino, Microwave Imaging. Hoboken, NJ, USA: Wiley, 2010.

- [3] M. Li, O. Semerci, and A. Abubakar, "A contrast source inversion method in the wavelet domain," *Inverse Prob.*, vol. 29, no. 2, 2013, Art. no. 025015.
- [4] H. M. Yao, W. E. I. Sha, and L. J. Jiang, "Applying convolutional neural networks for the source reconstruction," *Prog. Electromagn. Res. M*, vol. 76, pp. 91–99, 2018.
- [5] M. Li and A. Abubakar, "Electromagnetic inverse problems [guest editorial]," *IEEE Antennas Propag. Mag.*, vol. 59, no. 5, pp. 9–115, Oct. 2017.
- [6] J.-R. Regue, M. Ribo, J.-M. Garrell, and A. Martin, "A genetic algorithm based method for source identification and far-field radiated emissions prediction from near-field measurements for PCB characterization," *IEEE Trans. Electromagn. Compat.*, vol. 43, no. 4, pp. 520–530, Nov. 2001.
- [7] Y. Yu and L. Carin, "Three-dimensional Bayesian inversion with application to subsurface sensing," *IEEE Trans. Geosci. Remote Sens.*, vol. 45, no. 5, pp. 1258–1270, May 2007.
- [8] X. Song, M. Li, and A. Abubakar, "A regularization scheme based on Gaussian mixture model for EM data inversion," in *IEEE MTT-S Int. Microw. Symp. Dig.*, Hangzhou, China, Dec. 2020, pp. 1–4.
- [9] R. E. Kleinman and P. M. van den Berg, "Two-dimensional location and shape reconstruction," *Radio Sci.*, vol. 29, no. 4, pp. 1157–1169, Jul 1994
- [10] P. Li and L. J. Jiang, "Source reconstruction method-based radiated emission characterization for PCBs," *IEEE Trans. Electromagn. Compat.*, vol. 55, no. 5, pp. 933–940, Oct. 2013.
- [11] M. Li, A. Abubakar, T. M. Habashy, and Y. Zhang, "Inversion of controlled-source electromagnetic data using a model-based approach," *Geophys. Prospecting*, vol. 58, no. 3, pp. 455–467, May 2010.
- [12] P. Li, Y. Li, L. J. Jiang, and J. Hu, "A wide-band equivalent source reconstruction method exploiting the stoer-bulirsch algorithm with the adaptive frequency sampling," *IEEE Trans. Antennas Propag.*, vol. 61, no. 10, pp. 5338–5343, Oct. 2013.
- [13] H. M. Yao, L. Jiang, H. H. Zhang, and W. E. I. Sha, "Machine learning methodology review for computational electromagnetics," in *Proc. Int. Appl. Comput. Electromagn. Soc. Symp.*, vol. 1, Nanjing, China, Aug. 2019, pp. 1–4.
- [14] A. Massa, D. Marcantonio, X. Chen, M. Li, and M. Salucci, "DNNs as applied to electromagnetics, antennas, and propagation—A review," *IEEE Antennas Wireless Propag. Lett.*, vol. 18, pp. 2225–2229, 2019.
- [15] Y. LeCun, Y. Bengio, and G. Hinton, "Deep learning," *Nature*, vol. 521, no. 7553, pp. 436–444, May 2015.
- [16] H. M. Yao, L. J. Jiang, and Y. W. Qin, "Machine learning based method of moments (ML-MoM)," in *Proc. IEEE Int. Symp. Antennas Propag. USNC/URSI Nat. Radio Sci. Meeting*, San Diego, CA, USA, Jul. 2017, pp. 973–974.
- [17] T. Shan et al., "Study on a fast solver for Poisson's equation based on deep learning technique," *IEEE Trans. Antennas Propag.*, vol. 68, no. 9, pp. 6725–6733, Apr. 2020.
- [18] H. M. Yao, Y. W. Qin, and L. J. Jiang, "Machine learning based MoM (ML-MoM) for parasitic capacitance extractions," in *Proc. IEEE Electr. Design Adv. Packag. Syst. (EDAPS)*, Honolulu, HI, USA, Dec. 2016, pp. 171–173.
- [19] S. Chen, H. Wang, F. Xu, and Y.-Q. Jin, "Target classification using the deep convolutional networks for SAR images," *IEEE Trans. Geosci. Remote Sens.*, vol. 54, no. 8, pp. 4806–4817, Aug. 2016.
- [20] H. M. Yao, M. Li, and L. Jiang, "Applying deep learning approach to the far-field subwavelength imaging based on near-field resonant metalens at microwave frequencies," *IEEE Access*, vol. 7, pp. 63801–63808, 2019.
- [21] H. H. Zhang, L. J. Jiang, and H. M. Yao, "Embedding the behavior macromodel into TDIE for transient field-circuit simulations," *IEEE Trans. Antennas Propag.*, vol. 64, no. 7, pp. 3233–3238, Jul. 2016.
- [22] H. H. Zhang, L. J. Jiang, H. M. Yao, and Y. Zhang, "Transient heterogeneous electromagnetic simulation with DGTD and behavioral macromodel," *IEEE Trans. Electromagn. Compat.*, vol. 59, no. 4, pp. 1152–1160, Aug. 2017.
- [23] H. M. Yao, R. Guo, M. Li, L. Jiang, and M. K. P. Ng, "Enhanced supervised descent learning technique for electromagnetic inverse scattering problems by the deep convolutional neural networks," *IEEE Trans. Antennas Propag.*, vol. 70, no. 8, pp. 6195–6206, Aug. 2022.
- [24] R. Guo, Z. Lin, M. Li, F. Yang, S. Xu, and A. Abubakar, "A nonlinear model compression scheme based on variational autoencoder for microwave data inversion," *IEEE Trans. Antennas Propag.*, vol. 70, no. 11, pp. 11059–11069, Nov. 2022.

- [25] T. Shan, Z. Lin, X. Song, M. Li, F. Yang, and S. Xu, "A new approach for solving inverse scattering problems based on physics-informed supervised residual learning," in *Proc. 16th Eur. Conf. Antennas Propag.* (EuCAP), Mar. 2022, pp. 1–4.
- [26] H. M. Yao, L. Jiang, and W. E. I. Sha, "Source reconstruction method based on machine learning algorithms," in *Proc. Joint Int. Symp. Electromagn. Compat.*, Sapporo Asia–Pacific Int. Symp. Electromagn. Compat. (EMC Sapporo/APEMC), Jun. 2019, pp. 774–777.
- [27] X. Tong, D. W. P. Thomas, A. Nothofer, P. Sewell, and C. Christopoulos, "Modeling electromagnetic emissions from printed circuit boards in closed environments using equivalent dipoles," *IEEE Trans. Electro*magn. Compat., vol. 52, no. 2, pp. 462–470, May 2010.
- [28] H. M. Yao, L. Jiang, and M. Ng, "Implementing the fast full-wave electromagnetic forward solver using the deep convolutional encoderdecoder architecture," *IEEE Trans. Antennas Propag.*, vol. 71, no. 1, pp. 1152–1157, Jan. 2023.
- [29] M. Mirza and S. Osindero, "Conditional generative adversarial nets," 2014, arXiv:1411.1784.
- [30] P. Isola, J.-Y. Zhu, T. Zhou, and A. A. Efros, "Image-to-image translation with conditional adversarial networks," 2016, *arXiv:1611.07004*.
- [31] G. Antipov, M. Baccouche, and J. Dugelay, "Face aging with conditional generative adversarial networks," in *Proc. IEEE Int. Conf. Image Process. (ICIP)*, Sep. 2017, pp. 2089–2093.
- [32] I. Goodfellow et al., "Generative adversarial nets," in *Proc. NIPS*, 2014, pp. 1–9.
- [33] H. Zhang, V. Sindagi, and V. M. Patel, "Image de-raining using a conditional generative adversarial network," *IEEE Trans. Circuits Syst. Video Technol.*, vol. 30, no. 11, pp. 3943–3956, Nov. 2020.
- [34] G. Yang et al., "DAGAN: Deep de-aliasing generative adversarial networks for fast compressed sensing MRI reconstruction," *IEEE Trans. Med. Imag.*, vol. 37, no. 6, pp. 1310–1321, Jun. 2018.
- [35] F. Wuttke, H. Lyu, A. S. Sattari, and Z. H. Rizvi, "Wave based damage detection in solid structures using spatially asymmetric encoder–decoder network," Sci. Rep., vol. 11, no. 1, pp. 1–15, Oct. 2021.
- [36] I. A. Kazerouni, G. Dooly, and D. Toal, "Ghost-UNet: An asymmetric encoder-decoder architecture for semantic segmentation from scratch," *IEEE Access*, vol. 9, pp. 97457–97465, 2021.
- [37] N. Srivastava, G. Hinton, A. Krizhevsky, I. Sutskever, and R. Salakhutdinov, "Dropout: A simple way to prevent neural networks from overfitting," *J. Mach. Learn. Res.*, vol. 15, pp. 1929–1958, Sep. 2014.
- [38] H. M. Yao, W. E. I. Sha, and L. Jiang, "Two-step enhanced deep learning approach for electromagnetic inverse scattering problems," *IEEE Antennas Wireless Propag. Lett.*, vol. 18, pp. 2254–2258, 2019.
- [39] H. M. Yao, L. Jiang, and W. E. I. Sha, "Enhanced deep learning approach based on the deep convolutional encoder-decoder architecture for electromagnetic inverse scattering problems," *IEEE Antennas Wireless Propag. Lett.*, vol. 19, pp. 1211–1215, 2020.
- [40] Z. Wei and X. Chen, "Deep-learning schemes for full-wave nonlinear inverse scattering problems," *IEEE Trans. Geosci. Remote Sens.*, vol. 57, no. 4, pp. 1849–1860, Apr. 2019.
- [41] Z. Lin et al., "Low-frequency data prediction with iterative learning for highly nonlinear inverse scattering problems," *IEEE Trans. Microw. Theory Techn.*, vol. 69, no. 10, pp. 4366–4376, Oct. 2021.
- [42] R. Guo, X. Song, M. Li, F. Yang, S. Xu, and A. Abubakar, "Supervised descent learning technique for 2-D microwave imaging," *IEEE Trans. Antennas Propag.*, vol. 67, no. 5, pp. 3550–3554, May 2019.
- [43] R. Guo et al., "Pixel- and model-based microwave inversion with supervised descent method for dielectric targets," *IEEE Trans. Antennas Propag.*, vol. 68, no. 12, pp. 8114–8126, Dec. 2020.
- [44] K. H. Jin, M. T. McCann, E. Froustey, and M. Unser, "Deep convolutional neural network for inverse problems in imaging," *IEEE Trans. Image Process.*, vol. 26, no. 9, pp. 4509–4522, Sep. 2017.
- [45] J. Cong and B. Xiao, "Minimizing computation in convolutional neural networks," in *Proc. Int. Conf. Artif. Neural Netw.*, 2014, pp. 281–290.

- [46] M. F. Catedra, The CG-FFT Method: Application of Signal Processing Techniques to Electromagnetics. Boston, MA, USA: Artech House, 1995
- [47] P. Kim, MATLAB Deep Learning. New York, NY, USA: Apress, 2017.
- [48] D. P. Kingma and J. L. Ba, "Adam: A method for stochastic optimization," in *Proc. Int. Conf. Learn. Represent.*, 2015, pp. 1–41.
- [49] A. Afsari, A. M. Abbosh, and Y. Rahmat-Samii, "Adaptive beamforming by compact arrays using evolutionary optimization of Schelkunoff polynomials," *IEEE Trans. Antennas Propag.*, vol. 70, no. 6, pp. 4485–4497, Jun. 2022.
- [50] F. S. Marzano, S. Barbieri, G. Vulpiani, and W. I. Rose, "Volcanic ash cloud retrieval by ground-based microwave weather radar," *IEEE Trans. Geosci. Remote Sens.*, vol. 44, no. 11, pp. 3235–3246, Nov. 2006.
- [51] G. Longo, E. Russo, A. Armando, and A. Merlo, "Attacking (and defending) the maritime radar system," *IEEE Trans. Inf. Forensics Security*, vol. 18, pp. 3575–3589, 2023.
- [52] A. Benedetto, F. Tosti, L. B. Ciampoli, and F. D'Amico, "An overview of ground-penetrating radar signal processing techniques for road inspections," *Signal Process.*, vol. 132, pp. 201–209, Mar. 2017.
- [53] M. Salucci, M. Arrebola, T. Shan, and M. Li, "Artificial intelligence: New frontiers in real-time inverse scattering and electromagnetic imaging," *IEEE Trans. Antennas Propag.*, vol. 70, no. 8, pp. 6349–6364, Aug. 2022.
- [54] X. Chen, Z. Wei, M. Li, and P. Rocca, "A review of deep learning approaches for inverse scattering problems (invited review)," *Prog. Electromagn. Res.*, vol. 167, pp. 67–81, 2020.
- [55] Y. Zhong, M. Salucci, K. Xu, A. Polo, and A. Massa, "A multiresolution contraction integral equation method for solving highly nonlinear inverse scattering problems," *IEEE Trans. Microw. Theory Techn.*, vol. 68, no. 4, pp. 1234–1247, Apr. 2020.
- [56] M. Salucci, G. Oliveri, A. Randazzo, M. Pastorino, and A. Massa, "Electromagnetic subsurface prospecting by a multifocusing inexact Newton method within the second-order born approximation," *J. Opt. Soc. Amer. A, Opt. Image Sci.*, vol. 31, no. 6, p. 1167, Jun. 2014.
- [57] M. Hajebi and A. Hoorfar, "A multiscale optimization technique for large-scale subsurface profiling," *IEEE Geosci. Remote Sens. Lett.*, vol. 18, no. 10, pp. 1706–1710, Oct. 2021.
- [58] M. Hajebi and A. Hoorfar, "Multiple buried target reconstruction using a multiscale hybrid of diffraction tomography and CMA-ES optimization," *IEEE Trans. Geosci. Remote Sens.*, vol. 60, 2022, Art. no. 2006713.
- [59] M. Salucci et al., "Three-dimensional electromagnetic imaging of dielectric targets by means of the multiscaling inexact-Newton method," J. Opt. Soc. Amer. A, Opt. Image Sci., vol. 34, no. 7, pp. 1119–1131, Jul. 2017.
- [60] R. Song, Y. Huang, X. Ye, K. Xu, C. Li, and X. Chen, "Learning-based inversion method for solving electromagnetic inverse scattering with mixed boundary conditions," *IEEE Trans. Antennas Propag.*, vol. 70, no. 8, pp. 6218–6228, Aug. 2022.
- [61] M. Ambrosanio, S. Franceschini, F. Baselice, and V. Pascazio, "Machine learning for microwave imaging," in *Proc. 14th Eur. Conf. Antennas Propag. (EuCAP)*, Copenhagen, Denmark, Mar. 2020, pp. 1–4.
- [62] Y. Zhang, M. Lambert, A. Fraysse, and D. Lesselier, "Unrolled convolutional neural network for full-wave inverse scattering," *IEEE Trans. Antennas Propag.*, vol. 71, no. 1, pp. 947–956, Jan. 2023.
- [63] M. M. Autorino, S. Franceschini, M. Ambrosanio, F. Baselice, and V. Pascazio, "Deep learning strategies for quantitative biomedical microwave imaging," in *Proc. 16th Eur. Conf. Antennas Propag.* (EuCAP), Madrid, Spain, Mar. 2022, pp. 1–4.
- [64] C. Dachena et al., "Microwave imaging of the neck by means of artificial neural networks for tumor detection," *IEEE Open J. Antennas Propag.*, vol. 2, pp. 1044–1056, 2021.
- [65] J. Chani-Cahuana, C. Fager, and T. Eriksson, "Lower bound for the normalized mean square error in power amplifier linearization," *IEEE Microw. Wireless Compon. Lett.*, vol. 28, no. 5, pp. 425–427, May 2018.